

High-Performance Ge Quantum Dot Decorated Graphene/Zinc-Oxide Heterostructure Infrared Photodetector

Xiang Liu,^{†,‡,||} Xiangbing Ji,^{†,||} Mingju Liu,^{‡,||} Nianze Liu,[†] Zhi Tao,[†] Qing Dai,^{*,‡,§} Lei Wei,^{*,†} Chi Li,^{*,‡,§} Xiaobing Zhang,[†] and Baoping Wang[†]

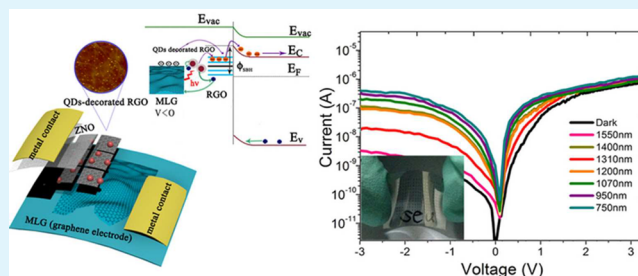
[†]Electronic Science and Engineering School, Southeast University, Nanjing 210096, China

[‡]National Center for Nanoscience & Technology, Beijing 100190, China

[§]London Center for Nanotechnology, University College London, London WC1H 0AH, United Kingdom

ABSTRACT: A novel size-controllable germanium quantum dot (Ge QD) is synthesized and decorated onto reduced graphene oxide (RGO) fragments to overcome the low infrared (IR) photoresponses (~ 0.1 A/W)^{13,14} of pristine graphene. With the integration of flexible substrate, monolayer graphene (MLG) electrode and n-type zinc oxide (ZnO), a high-performance QD-decorated-RGO/ZnO heterostructure infrared photodetector is reported in this study. The Ge QD-decorated-RGO hybrid photosensitive composite improves the responsivity (~ 9.7 A/W, 1400 nm) in IR waveband without sacrificing the response speed (~ 40 μ s rise time and 90 μ s recovery time). In addition, the effective barrier formed between graphene and ZnO interface restricts the dark current (~ 1.4 nA, -3 V) to guarantee the relatively excellent rectifying behavior and high on/off ratio ($\sim 10^3$) for this IR photodetector. With these superior inherent properties and micron-sized sensing active area, this photodetector manifests great potential in the future application of graphene-based IR photodetector.

KEYWORDS: germanium quantum dots, infrared photodetector, flexible, micron-size device, graphene/zinc-oxide heterostructure



1. INTRODUCTION

Cost-effective group IV semiconductors including Ge and Si have been greatly developed in the fabrication of conventional optoelectronics devices during past several decades.^{1–4} However, when the future interface technology—quantum dots—began to attract many researchers' interests, too much emphasis has been put on the II–VI Cd-based, IV–VI Pb-based, III–V In, Ga-based compound quantum dots (PbS,⁵ CdSe,⁶ PbSe,⁷ InAs⁸) due to their wavelength-tunable emission, strong absorption toward the incident light, and long electron–hole recombination lifetime.⁹ The nontoxic group IV semiconductors Ge and Si quantum dots with similar characteristics are great candidates to substitute the above cytotoxic heavy metal quantum dots. Especially on account of the larger excitonic Bohr radius (11.5 nm) and narrower band gap (0.67 eV) compared with those of silicon (4.9 nm excitonic Bohr radius, and 1.12 eV), germanium quantum dots can exhibit more quantum confinement effects^{10,11} and extend the spectral range to infrared (IR) waveband (850–1800 nm) in optoelectronic applications such as IR light emitting diode and IR photodetector. Moreover, with the coupling of graphene, the hottest two-dimensional (2D) atomic material, the alternative Ge quantum dot/graphene systematic composite can avoid the limited charge mobility in quantum dot films¹² and the low infrared (IR) photoresponses (less than 0.1A/W) of pristine graphene.^{13,14}

Nevertheless, the conventional Ge quantum dot synthesis method relies on the in situ growth formation method with high temperature (>700 °C) and sophisticated layer-by-layer processes (such as molecular beam epitaxy,¹⁵ high-temperature RF sputtering, and annealing), which are usually utilized in the integration of InP, InAs, and InGaAs IR emission quantum dots.⁸ Considering the natural thermal instability of flexible substrate and graphene electrode, these fabrication methods cannot be employed in the future flexible IR photodetectors.

In this study, size-tunable colloid Ge QDs solution, which can be transferred on a large scale, was synthesized through an aqueous chemical etching method and then integrated into the graphene-based flexible IR photodetector. To explore an optimal fabrication process and operating structure, we designed two different photodetectors and contrasted them under the same experimental ambient. In this regard, performances such as photocurrent, responsivity, rectifying capability, and response time of each device were measured and characterized. In addition, two different mechanisms that led to the distinct properties of these two devices were also elucidated in this study.

Received: October 18, 2014

Accepted: January 5, 2015

Published: January 5, 2015

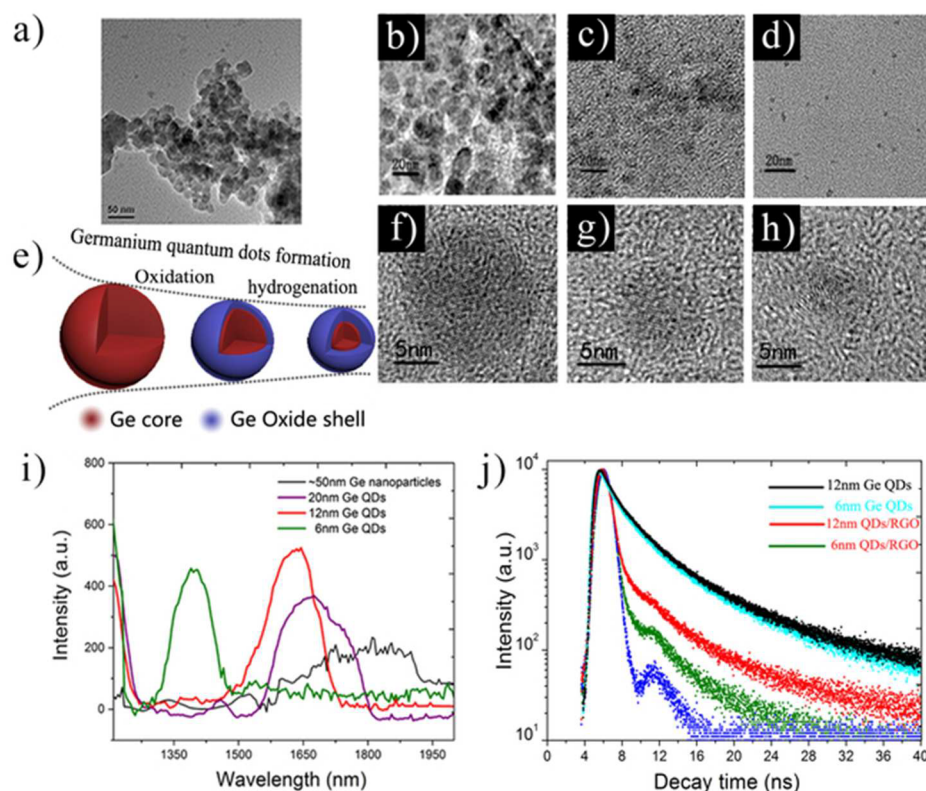


Figure 1. Characterization of Ge QD material. (a) TEM image of Ge nanoparticle precursor solution. TEM image of (b–d) large-scale and (f–h) detailed Ge QDs. (e) Schematic of the Ge QDs formation process. (i) The IR photoluminescence (PL) spectrum of different size Ge QDs. (j) Transient time-resolved fluorescence decay of the contrasted Ge QDs with different size and oxide shell.

2. EXPERIMENTAL SECTION

2.1. Synthesis of Bulk Ge Nanoparticle Solution. Germanium precursor solution was prepared by reported typical reduction method.^{10,11,16} The synthesis process of Ge nanoparticles is described as following: (1) Under inert atmosphere, GeO_2 powder (1g, sigma-aldrich) was dissolved in 50 mL ammonium hydroxide solution in an ultrasonic machine heated to 70 °C. (2) Oxidation–reductant NaBH_4 diluted with 50 mL DI-water (5 mol/L) was then injected. The reaction mixture solution stood for approximately 12 h, and the solution changed from transparent to germanium red. (3) At ~ -8 °C, the reaction product was transferred to a centrifuge tube and centrifuged to obtain the precipitate. (4) The same amount of methanol was added to obtain the Ge nanoparticle precursor solution (diameter, 40–60 nm; in Figure 1a).

2.2. Chemical Wet-Etching Method Forming Size-Tunable Colloid $\text{Ge}/\text{Ge}_x\text{O}_y\text{H}_z$ Core/Shell QDs. Chemical wet-etching method has been utilized in the synthesis of another group IV semiconductor silicon QDs in previous reports.^{17–20} The obtained germanium nanoparticles were reduced to Ge QDs using etching buffer solution (mixed with hydrofluoric acid (HF) and nitric acid (HNO_3)). Then, 69 wt % HNO_3 and 46 wt % HF mixed etching buffer solution (1:4 v/v) was added to the Ge nanoparticle dilution. The chemical etching reaction was operated in the ultrasonic machine, which played a vital role in promoting the uniformity of the Ge quantum dots after the reaction. The etching solution was obtained by micropipette, which was used to add the etching solution dropwise to the reaction polytetrafluoroethylene (PTFE) beaker in 2 μL quantities every 10 s. The etching time was controlled from 10 to 40 min and the approximate QD diameter was determined through this method (Figure 1b–d,f–h). Finally, the obtained $\text{Ge}/\text{Ge}_x\text{O}_y\text{H}_z$ QDs solution was filtered by 0.1 μm filter (polyvinylidene fluoride (PVDF)) and collected after drying in a drying-off oven.

2.3. Preparation of Graphene and Device Fabrication Process. Hummer's method grown graphene oxide (GO) was

purchased to be reverted to reduced graphene oxide (RGO) with ~ 20 μm diameter through the reduction process by oxidation–reductant NaBH_4 . The PET substrate (transmission wavelength, 300–2500 nm) with monolayer graphene was purchased from Suzhou Nord Derivatives Pharm-Tech Co., Ltd. After that, thin-layer Au was deposited on the edge of the graphene as the metal contact. Then, two different structured photodetectors (PDs) were fabricated by as-prepared Ge QDs alone and Ge-QD-decorated graphene, respectively. Briefly, 4 mg/mL Ge QDs methanol solution was spin coated (1000 r/min) on the PET graphene substrate, dried and annealed in a vacuum chamber at 200 °C. And this spin-coating process with low temperature annealing treatment was repeated 2 times to form ~ 50 nm Ge QDs layer. The hybrid Ge QDs/graphene solution was made up of 1 mL of 5 mg/mL Ge QDs and 1 mL of 1 mg/mL RGO solution. The hybrid solution was filtered through membrane filter to obtain the QD-decorated RGO. The hybrids would be added to the PET graphene substrate by drop-cast process and were annealed at 190 °C to bond QDs on RGO surface. Finally, room-temperature RF-magnetron sputtering was carried out to deposit ~ 30 nm n type-ZnO and another thin layer Au metal contact (150 \times 200 μm) using alignment deposition metal mask (presion, 10 μm). They were combined with the graphene electrode to sandwich the Ge QDs and QD-decorated-RGO respectively.

2.4. Characterization of As-Prepared Materials and Devices. The size-tunable $\text{Ge}/\text{Ge}_x\text{O}_y\text{H}_z$ QDs samples were characterized by Transmission electron microscope (TEM, Tecnai G2 F20 U-TWIN) and QD-decorated RGO was characterized by scanning electron microscope (SEM, Hitachi S4800). Atomic force microscope (AFM, Multimode-8-AM) was used to characterize two different structure devices' interfaces. Meanwhile, the photoluminescence curve was obtained by LSS5 (PerkinElmer Instruments Co., Ltd.) and time-resolved spectrofluorometer (FL3-21-IHR320-TCSPC) was the testing spectrometer to investigate the charge transfer between $\text{Ge}/\text{Ge}_x\text{O}_y\text{H}_z$ QDs and RGO fragments. All the graphene material Raman spectrum was swept out by Raman spectroscopy (inVia). The light-

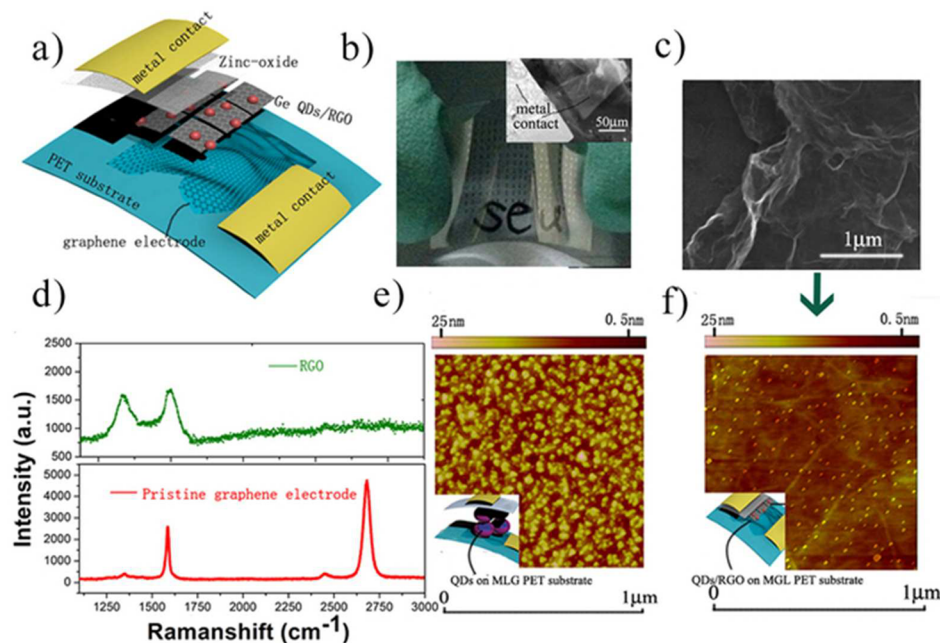


Figure 2. Characterization of the flexible IR photodetectors. (a) Structure schematic of the QD-decorated-RGO/ZnO heterostructure photodetector. (b) Overall optical photography of the flexible IR photodetectors and (inset) SEM image of the detector unit. (c) SEM image of the QDs/RGO hybrid on the MLG substrate. (d) Raman spectrum for RGO and MLG. (e) Surface detail of the one-step spin-coating/annealed Ge QDs film (~ 25 nm) on the MLG (PET substrate) and (inset) structure schematic of the device. (f) AFM image of the QD-decorated-RGO surface after the annealed bonding and (inset) structure schematic of the device.

bias was applied by the power-adjustable LED lamp and the power density of the device planar was measured by multiwavelength optic intensitometer DES-100H (U.S.A SP Co.Ltd.). The electric character was tested using a Keithley 4200 and oscilloscope (National Instrument, DSA91304A) was set in the device testing loop to get the pulse photocurrent response.

3. RESULT AND DISCUSSION

According to the high-resolution TEM image of the large-scale and detailed Ge QDs in Figure 1b–d,f–h, the diameters and errors of the QDs in each image were approximately $18 \text{ nm} \pm 1$ (5 min etching time), $12 \text{ nm} \pm 0.5$ (10 min etching time), and $6 \text{ nm} \pm 0.25$ (20 min etching time), respectively. Figure 1e depicts the chemical etching process to form the Ge oxide shell and two chemical steps (oxidation by HNO_3 and hydrogenated by HF) in the Germanium surface. These reactions can be summarized as follows: $3\text{Ge} + 4\text{HNO}_3 \rightarrow 3\text{GeO}_2 + 4\text{NO} + 2\text{H}_2\text{O}$ and $\text{GeO}_2 + 6\text{HF} \rightarrow \text{H}_2\text{GeF}_6 + 2\text{H}_2\text{O}$. Therefore, as the etching time (at the same concentration) increases, the size of the Ge QDs gradually declines, which makes the Ge QDs convert to the Ge/Ge oxide structure. Furthermore, the thickness of the formed Ge oxide shell augments gradually accompanied by longer etching time.

The IR photoluminescence (PL) and time-resolved fluorescence decay were measured to characterize the photonic properties of the Ge QDs and the charge transfer between RGO and Ge/Ge oxide at room temperature in Figure 1j. Though the bulk germanium material has weak absorbance in infrared waveband, Ge QDs enhance the absorbance and photoluminescence in near-infrared waveband by reason for the quantum confinement and tensile strain.^{10,11} Due to the relatively long excitonic Bohr radius (11.5 nm) of Ge material, Ge QDs will show a stronger quantum confinement when their diameter approaches 11.5 nm (as seen from the PL emission curve in Figure 1i). Figure 1j exhibits the emission decay

kinetics of different size Ge/Ge oxide QDs and QDs/RGO samples. A carrier quench occurred in the interface between QDs and RGO, as shown in Figure 1j. The exponentially fitted time constant referred to the radiative excitation lifetime is $\tau = 3.4, 2.8, 0.56,$ and 0.37 ns for 12 and 6 nm Ge QDs and 12 and 6 nm QDs/RGO hybrids, respectively. The charge transfer or energy transfer between the 12 nm QDs (thinner Ge oxide shell) and RGO is more efficient than that of the 6 nm QDs (thicker Ge oxide shell), which has been proved in previous reports that more trap states in the thicker shell QDs can hamper the radiative recombination of holes and electrons.^{21,22} Therefore, on the premise of better absorbance in the IR waveband and the effective charge transfer, 12 nm QDs were chosen to be integrated onto this device to guarantee the optimal device performance.

Figure 2a demonstrates the schematic diagram of the as-fabricated QD-decorated-RGO/ZnO heterostructure device. The fabrication process has been described in the Experimental Section. Furthermore, we prepared the patterns on the flexible PET substrate through lithography, as depicted in Figure 2b. Figure 2d compares the Raman spectrum of RGO and pristine graphene electrode. On one hand, the 2D band peak at around 2650 cm^{-1} , G band peak at 1550 cm^{-1} and a nearly 2:1 I_{2D}/I_G ratio certify the crystal quality of our monolayer graphene (MLG) electrode.²³ The MLG electrode set here has two benefits for this device: first, MLG has lower incident light loss (2–3%) due to its low sheet resistance and high transparency compared with ITO ($\sim 22\%$); second, the barrier between MLG and RGO can be ignored considering that they are all “graphene” with the same work function which can supply a high charge collection efficiency. On the other hand, in the spectrum of RGO, the peak and intensity of G band and 2D band is shifted, indicating the existing of defect states in graphene.^{13,14} Figure 2e presents the morphology of MLG film

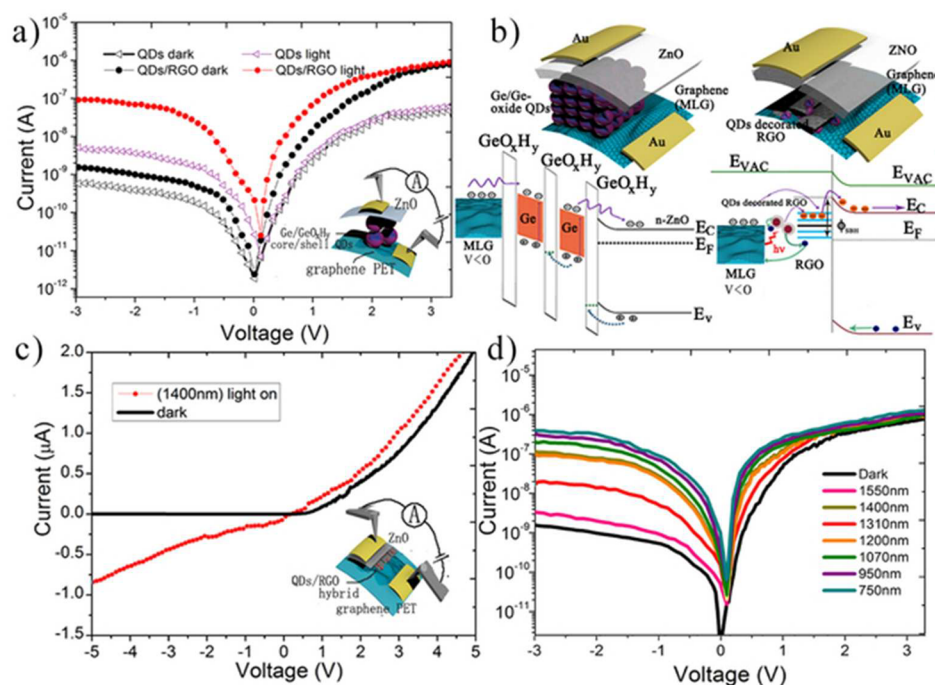


Figure 3. Characterization of photodetector's opto-electric performance. (a) Photocurrents of the two different representative devices upon IR 1400 nm incident light illumination. (b) Energy band and bias mechanism schematic diagram of the two devices. (c) The linear I - V curve of the QD-decorated-RGO/ZnO heterostructure under dark and 1400 nm illumination to show the rectifying behavior of the device. (d) Photocurrent variation of the QD-decorated-RGO/ZnO device exposed to the different wave incident IR light.

deposited by Ge QDs directly, while the hybrids of Ge QDs and RGO are characterized in Figure 2c and f observed from SEM and AFM.

Without the RGO fragments, the two-terminal device with encapsulated Ge/Ge-Oxide QDs operates like a metal-oxide-semiconductor (MOS) structure PD (Figure 2e, inset).^{24–26,36} However, after blending the Ge QDs with RGO fragments, because the radius of RGO fragments ($\sim 20 \mu\text{m}$) is much larger than that of Ge QDs (Figure 2c), Ge QDs were only distributed on the RGO surface discretely (Figure 2f), causing a direct contact between RGO and n-type ZnO. The rectifying behavior of this device can be observed in Figure 3 a,c,d as a result of the effective barrier in this contact interface. In this RGO/ZnO interface, a Schottky barrier is formed, given that the work function of RGO ($W_{\text{RGO}} = 4.5 \text{ eV}$) is greater than the electron affinity of semiconduction ZnO ($\chi \sim 4.1 \text{ eV}$).²⁷ The height of Schottky barrier (ϕ_{SBH}) can be expressed by the following equation:²⁸

$$\phi_{\text{SBH}} = W_{\text{RGO}} - \chi \quad (1)$$

To investigate the photocurrent contribution of RGO, we compared the photocurrent of these two different representative devices upon IR 1400 nm incident light (Figure 3a). It can be clearly seen that the photocurrent of QDs/RGO hybrids device ($0.1 \mu\text{A}$) is approximately 2 orders of magnitude greater than that of QDs (4 nA) at -3 V reverse bias even though less Ge QDs are utilized in QDs/RGO structure, which can be seen in Figure 2e,f, Ge QDs in panel f are much more sparse than those in panel e.

Different mechanisms for these two devices are illustrated in Figure 3b. In the MOS structure, photogenerated carriers have to tunnel through the entire Ge oxide layer to reach electrodes (Figure 2b, left).^{24–26} However, in the RGO/ZnO structure, photogenerated carriers are transferred to the graphene surface

and then driven to the electrodes (Figure 2b, right). Thus, four possible hypotheses are proposed to explain the relatively higher photocurrent gain of the QD-decorated-RGO/ZnO heterostructure device: (1) The more effective photogenerated carrier causes separation in the QDs/RGO hybrids.²⁹ (2) Compared with the ultrafast mobility of graphene, the limited carrier mobility of Ge QDs will constrain the photocurrent in MOS structure. (3) Coulomb blockade effects in the Ge QDs can hamper the further increase of the electron transfer in the QDs layer. Especially for the QDs which are not located on the MLG electrode, it is difficult to transfer their photoexcited electrons to the electrode terminal across massive other QDs. (4) Under incident light, the Schottky barrier for electrons diminishes,^{30–33} which facilitates the charge drifting from RGO to ZnO at reverse bias. On the contrary, the barrier of MOS structure is insensitive at reverse bias.^{24,25} A possible reason for this phenomenon is the offset tunneling barrier of Ge oxide shell for electrons and holes (0.7 eV for electrons, 4.3 eV for holes).³⁴ Another impact element is that electrons are much more mobile than holes because of their lower tunneling mass. Consequently, because many more electrons than holes are transferred to the RGO, deep electron-doping is caused in RGO, and the barrier for electrons' drifting from RGO to ZnO is reduced at reverse voltage. Finally, we can rule out the influence of the photogenerated carriers from ZnO in IR waveband considering its wide bandgap ($\sim 3.3 \text{ eV}$).

To quantify the rectifying behavior of the device in Figure 3c, the current (I) passing through the Schottky barrier is described in the following equations:³⁵

$$I = I_{\text{sat}} \left[\exp\left(\frac{qV}{\eta kT}\right) - 1 \right] \quad (2)$$

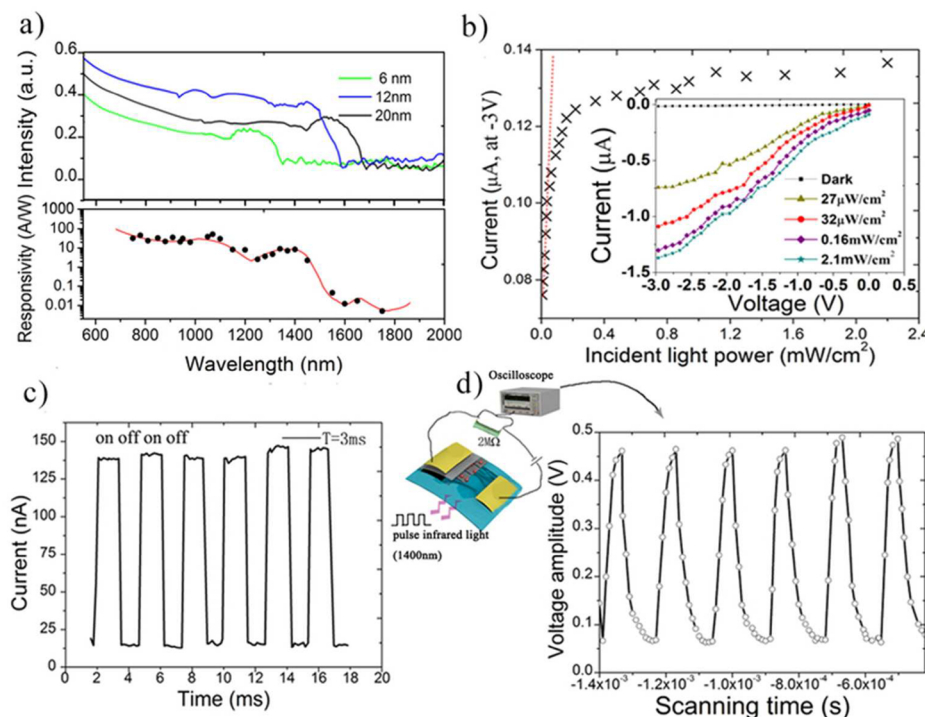


Figure 4. Characterization of the photodetector's detection performance and dynamic photoresponse to the pulsed IR light signal. (a) Responsivity of the device under different wavelength correlating to the absorption curve of the Ge QDs (at $32 \mu\text{W}/\text{cm}^2$ and -3 V reverse voltage). (b) Photocurrent versus luminous power density at -3 V reverse voltage and (inset) I - V characters curve under representative power density. (c) On/off performance of the device under $T = 3 \text{ ms}$ IR signal. (d) The schematic image of (left) the testing loop and (right) the rise/fall photocurrent response to a microsecond IR signal.

$$I_{\text{sat}} = AA^*T^2 \exp\left(-\frac{q\phi_{\text{SBH}}}{\eta kT}\right) \quad (3)$$

where I_{sat} is the saturation current, A , T , q , k , and η ($= (q/kT) dV/d \ln I_d$),²⁸ are the Schottky contact area, room temperature (300 K), electron charge, Boltzmann constant, and the ideality factor, respectively. A^* is the Richardson constant, which is $32 \text{ A cm}^{-2} \text{ K}^{-2}$ for ZnO.³⁵

Using these two equations and the experimental $I_{\text{dark}}-V$ curve in Figure 3c, the corresponding Schottky height is calculated as 0.665 eV. The ideality factor η is 5.24, while the normal range of η is between 1 and 2, which is aroused from the defects in RGO and the interface between RGO and ZnO, such as dislocations, vacancies, and impurities. Theoretically, it would be improved with the substantial increase of annealing temperature.^{28,37} However, the relatively low annealing temperature ($200 \text{ }^\circ\text{C}$) determined by the temperature instability of PET flexible substrate ($<220 \text{ }^\circ\text{C}$) limited the further improvement through this method. Besides, the QD density is another determinant affecting the contact between RGO and ZnO. Because the QDs and RGO are randomly distributed with each other, inevitably, there may exist some QDs that are in direct contact with ZnO. Electrons in these QDs have to tunnel through the dielectric GeO_2 shell when transferring to ZnO. Additionally, the Fermi-level position in a different part of RGO is also unpredictable due to different reduction level (Figure 3b). In sum, the effective barrier between RGO and ZnO actually is a combination of various effects, including Schottky barrier, tunneling barrier, surface defects, and different position of Fermi-level.

To further analyze the electrical performance of the QD-decorated-RGO/ZnO heterostructure device, photocurrents of

different wavelengths were measured under an incident light power of $32 \mu\text{W}/\text{cm}^2$ (Figure 3d). The device on/off ratio at reverse bias is much higher compared with that at forward bias owing to the decrease of effective electron barrier as mentioned above under illumination compared with its counterpart.

According to the statistics in Figure 3d, responsivities of this device were calculated using the following equation:

$$R(\text{AW}^{-1}) = \frac{I_p}{P_{\text{opt}}} \quad (4)$$

where I_p is photocurrent, and P_{opt} is the incident optical power (obtained by the light intensity multiplies the area). Given by an active area of $150 \times 200 \mu\text{m}$, the calculated responsivities at different IR wavebands are shown in Figure 4a at the same conditions (luminous power density: $32 \mu\text{W}/\text{cm}^2$ and -3 V reverse voltage). Both the photocurrents in Figure 3d and responsivities in Figure 4a indicate a fluctuating decrease from near IR waveband (800 nm) to middle IR waveband (1800 nm) and a relative extremum between 1300 and 1450 nm IR wavelengths. The responsivity at 1400 nm, which is near the extremum, is obtained at 9.7 A/W given by its P_{opt} ($9.6 \times 10^{-9} \text{ W}$) and a $9.3 \times 10^{-8} \text{ A}$ photocurrent. Additionally, according to Figure 4a, the photocurrent data correlates with the QDs absorption spectrum, which certifies the amplification of photocurrent in our device is primarily driven by the absorption of Ge QDs rather than RGO. Furthermore, on the basis of the above hypothesis, effective electron barrier nearly remains unchanged because unexcited QDs are unable to transfer charges onto RGO interface, which can explain the phenomenon that photocurrent declines dramatically and difficult to be measured beyond the absorption of Ge QDs.

If we consider only the noise from dark current, the detectivity of a given PD can be quantified by the following equation:

$$D^* = \frac{A^{1/2}R}{(2eI_{\text{dark}})^{1/2}} \quad (5)$$

where e is the elementary charge, A is the active area, I_{dark} is the dark current and R is the responsivity. The detectivity (dark current, 1.4 nA) of RGO/ZnO heterostructure PD is 7.98×10^{12} Jones under 1400 nm IR light illumination and -3 V reverse bias. To compare the device performances before and after optimization, the responsivity (0.47 A/W) and detectivity (6.42×10^{11} Jones) of the MOS structure PD were also estimated according to the statistics in Figure 3a (1400 nm IR region, -3 V reverse voltage, $32 \mu\text{W}/\text{cm}^2$) following formulas 4 and 5. Consequently, the overall performance of the PD is greatly ameliorated after the introduction of RGO.

Figure 4b demonstrates the relationship between photocurrent and luminous power intensity, while the inset portrays photocurrent versus bias voltage under four different light intensities. The increase of photocurrent almost keep linear under the faint incident light intensity but gradually reaches a saturation state resulting from all the discrete Ge QDs on the RGO surface being sufficiently excited.

Finally, the on/off performance and response speed of this photodetector under reverse bias (-3 V) were investigated (Figure 4c and d), where FPGA-cored LED driving circuit was used to generate the pulsed light signal. Under the illumination of 3 ms period IR light signal (1400 nm, $\sim 32 \mu\text{W}/\text{cm}^2$), the device showed a rapid response to this on/off modulation measured by source meters. Herein, a 2 M Ω series resistance was set in the testing loop with a oscilloscope to probe the transient photocurrent under a microsecond pulsed IR signal light source (the same peak power density, $32 \mu\text{W}/\text{cm}^2$). As shown in Figure 4d, when the period was tuned at 170 μs by the control circuit, the photocurrent showed a "just enough" on/off response, where rise time (τ_r) and fall time (τ_f) were estimated to be around 40 and 90 μs , respectively. The fast response time is attributed to the enhanced charge separation of the QDs/RGO hybrid²⁹ and effective charge transfer on Ge/RGO interface,^{28,37} as shown in Figure 1j. However, the dynamic photoresponse time is much slower compared with this ultrafast QD emission quenching time (Figure 1j), which suggests the time of the charge transfer between RGO and QDs is not the most impact determinant in the photoresponse time. We supposed that the electron transfer barrier between RGO and ZnO will not disappear instantaneously after the illumination. It is because that the electrons from QDs accumulated on RGO need certain accumulation times to reach enough electron-doping level and curtail the effective barrier sufficiently. Even so, due to the microsecond level accumulation time, this device's response time is still much shorter than those of some other graphene based or QDs-base devices, such as graphene/ZnO nanorod array³¹ and graphene/PbS QDs FET.³⁸

In conclusion, we have demonstrated a novel micron-sized QD-decorated-RGO/ZnO heterostructure photodetector. Additionally, the effective electron barrier formed at the interface of the QD-decorated-RGO/ZnO heterostructure endows this device with a good rectifying behavior in the dark ambient and excellent photoresponse under illumination. The combination of the following five key features makes this device stand out

from the others: environmentally friendly materials, high responsivity, high on/off ratio, fast response time, and flexible substrate. All these results suggest that this photodetector can be a potential candidate for the future application in near-IR detection field.

AUTHOR INFORMATION

Corresponding Authors

*E-mail: daiq@nanocr.cn.

*E-mail: lw@seu.edu.cn.

*E-mail: lichi@nanocr.cn.

Author Contributions

||These authors contributed equally to this work.

Notes

The authors declare no competing financial interest.

ACKNOWLEDGMENTS

This work was supported in part by the National Key Basic Research Program 973 (2010CB327705), the National Natural Science Foundation Project (51120125001, 51350110232, 61372030, and 91333118), the Foundation of Doctoral Program of Ministry of Education (20120092120025), and the Research Fund for International Young Scientists from NSFC (51050110142, 61150110167, and 51150110160).

REFERENCES

- (1) Michel, J.; Liu, J.; Kimerling, L. C. High-Performance Ge-on-Si Photodetectors. *Nat. Photonics* **2014**, *4*, 527–534.
- (2) Yan, C.; Singh, N.; Cai, H.; Gan, C. L.; Lee, P. S. Network-Enhanced Photoresponse Time of Ge Nanowire Photodetectors. *ACS Appl. Mater. Interfaces* **2010**, *2*, 1794–1797.
- (3) Almeida, V. R.; Barrios, C. A.; Panepucci, R. R.; Lipson, M. All-Optical Control of Light on a Silicon Chip. *Nature* **2004**, *431*, 1081–1084.
- (4) Hirschman, K. D.; Tsybeskov, L.; Duttagupta, S. P.; Fauchet, P. M. Silicon-Based Visible Light-Emitting Devices Integrated into Microelectronic Circuits. *Nature* **1996**, *384*, 338–341.
- (5) Konstantatos, G.; Badioli, M.; Gaudreau, L.; Osmond, J.; Bernechea, M.; de Arquer, F. P. G.; Gatti, F.; Koppens, F. H. L. Hybrid Graphene-Quantum Dot Phototransistors with Ultrahigh Gain. *Nat. Nanotechnol.* **2012**, *7*, 363–368.
- (6) Nguyen, K. T.; Li, D.; Borah, P.; Ma, X.; Liu, Z.; Zhu, L.; Grüner, G.; Xiong, Q.; Zhao, Y. Photoinduced Charge Transfer within Polyaniline-Encapsulated Quantum Dots Decorated on Graphene. *ACS Appl. Mater. Interfaces* **2013**, *5*, 8105–8110.
- (7) Sun, Z.; Liu, Z.; Li, J.; Tai, G. A.; Lau, S. P.; Yan, F. Infrared Photodetectors Based on CVD-Grown Graphene and PbS Quantum Dots with Ultrahigh Responsivity. *Adv. Mater.* **2012**, *24*, 5878–5883.
- (8) İkpı, M. E.; Atkinson, P.; Bremner, S. P.; Ritchie, D. A. Fabrication of a Self-Aligned Cross-Wire Quantum-Dot Chain Light Emitting Diode by Molecular Beam Epitaxial Regrowth. *Nanotechnology* **2012**, *23*, 225304.
- (9) Liu, X.; Yang, X.; Liu, M.; Tao, Z.; Dai, Q.; Wei, L.; Li, C.; Zhang, X.; Wang, B.; Nathan, A. Photo-Modulated Thin Film Transistor Based on Dynamic Charge Transfer within Quantum-Dots-InGaZnO Interface. *Appl. Phys. Lett.* **2014**, *104*, 113501.
- (10) Wu, J.; Sun, Y.; Zou, R.; Song, G.; Chen, Z.; Wang, C.; Hu, J. One-Step Aqueous Solution Synthesis of Ge Nanocrystals from GeO₂ Powders. *CrystEngComm* **2011**, *13*, 3674.
- (11) Lee, D. C.; Pietryga, J. M.; Robel, I.; Werder, D. J.; Schaller, R. D.; Klimov, V. I. Colloidal Synthesis of Infrared-Emitting Germanium Nanocrystals. *J. Am. Chem. Soc.* **2009**, *131*, 3436–3437.
- (12) Geng, X.; Niu, L.; Xing, Z.; Song, R.; Liu, G.; Sun, M.; Cheng, G.; Zhong, H.; Liu, Z.; Zhang, Z.; Sun, L.; Xu, H.; Lu, L.; Liu, L. Aqueous-Processable Noncovalent Chemically Converted Graphene-

Quantum Dot Composites for Flexible and Transparent Optoelectronic Films. *Adv. Mater.* **2010**, *22*, 638–642.

(13) Chang, H.; Sun, Z.; Saito, M.; Yuan, Q.; Zhang, H.; Li, J.; Wang, Z.; Fujita, T.; Ding, F.; Zheng, Z.; Yan, F.; Wu, H.; Chen, M.; Ikuhara, Y. Regulating Infrared Photoresponses in Reduced Graphene Oxide Phototransistors by Defect and Atomic Structure Control. *ACS Nano* **2013**, *7*, 6310–6320.

(14) Chitara, B.; Panchakarla, L. S.; Krupanidhi, S. B.; Rao, C. N. R. Infrared Photodetectors Based on Reduced Graphene Oxide and Graphene Nanoribbons. *Adv. Mater.* **2011**, *23*, 5419–5424.

(15) Tong, S.; Liu, J. L.; Wan, J.; Wang, K. L. Normal-Incidence Ge Quantum-Dot Photodetectors at 1.5 μm Based on Si Substrate. *Appl. Phys. Lett.* **2002**, *80*, 1189.

(16) Wu, H. P.; Liu, J. F.; Wang, Y. W.; Zeng, Y. W.; Jiang, J. Z. Preparation of Ge Nanocrystals via Ultrasonic Solution Reduction. *Mater. Lett.* **2006**, *60*, 986–989.

(17) Kang, Z.; Liu, Y.; Tsang, C. H. A.; Ma, D. D. D.; Fan, X.; Wong, N. B.; Lee, S. T. Water-Soluble Silicon Quantum Dots with Wavelength-Tunable Photoluminescence. *Adv. Mater.* **2009**, *21*, 661–664.

(18) Kang, Z. H.; Tsang, C. H. A.; Wong, N. B.; Zhang, Z. D.; Lee, S. T. Silicon Quantum Dots: A General Photocatalyst for Reduction, Decomposition, and Selective Oxidation Reactions. *J. Am. Chem. Soc.* **2007**, *129*, 12090–12091.

(19) Kang, Z. H.; Tsang, C. H. A.; Zhang, Z. D.; Zhang, M. L.; Wong, N. B.; Zapien, J. A.; Shan, Y. Y.; Lee, S. T. A Polyoxometalate-Assisted Electrochemical Method for Silicon Nanostructures Preparation: From Quantum Dots to Nanowires. *J. Am. Chem. Soc.* **2007**, *129*, 5326–5327.

(20) Sato, K.; Tsuji, H.; Hirakuri, K.; Fukata, N.; Yamauchi, Y. Controlled Chemical Etching for Silicon Nanocrystals with Wavelength-Tunable Photoluminescence. *Chem. Commun.* **2009**, 3759–3761.

(21) Zhao, H.; Fan, Z.; Liang, H.; Selopal, G. S.; Gonfa, B. A.; Jin, L.; Soudi, A.; Cui, D.; Enrichi, F.; Natile, M. M.; Concina, I.; Ma, D.; Govorov, A. O.; Rosei, F.; Vomiero, A. Controlling Photoinduced Electron Transfer from PbS@CdS Core@Shell Quantum Dots to Metal Oxide Nanostructured Thin Films. *Nanoscale* **2014**, *6*, 7004.

(22) Greaney, M. J.; Das, S.; Webber, D. H.; Bradforth, S. E.; Brutchey, R. L. Improving Open Circuit Potential in Hybrid P3HT:CdSe Bulk Heterojunction Solar Cells via Colloidal Tert-butylthiol Ligand Exchange. *ACS Nano* **2012**, *6*, 4222–4230.

(23) Cançado, L. G.; Jorio, A.; Ferreira, E. H. M.; Stavale, F.; Achete, C. A.; Capaz, R. B.; Moutinho, M. V. O.; Lombardo, A.; Kulmala, T. S.; Ferrari, A. C. Quantifying Defects in Graphene via Raman Spectroscopy at Different Excitation Energies. *Nano Lett.* **2011**, *11*, 3190–3196.

(24) Cosentino, S.; Liu, P.; Le, S. T.; Lee, S.; Paine, D.; Zaslavsky, A.; Pacifici, D.; Mirabella, S.; Miritello, M.; Crupi, I.; Terrasi, A. High-Efficiency Silicon-Compatible Photodetectors Based on Ge Quantum Dots. *Appl. Phys. Lett.* **2011**, *98*, 221107.

(25) Liu, P.; Cosentino, S.; Le, S. T.; Lee, S.; Paine, D.; Zaslavsky, A.; Pacifici, D.; Mirabella, S.; Miritello, M.; Crupi, I.; Terrasi, A. Transient Photoresponse and Incident Power Dependence of High-Efficiency Germanium Quantum Dot Photodetectors. *J. Appl. Phys.* **2012**, *112*, 083103.

(26) Shieh, J. M.; Lai, Y. F.; Ni, W. X.; Kuo, H. C.; Fang, C. Y.; Huang, J. Y.; Pan, C. L. Enhanced Photoresponse of a Metal-Oxide-Semiconductor Photodetector with Silicon Nanocrystals Embedded in the Oxide Layer. *Appl. Phys. Lett.* **2007**, *90*, 051105.

(27) Lee, S.; Lee, Y.; Kim, D. Y.; Song, E. B.; Kim, S. M. Back-Gate Tuning of Schottky Barrier Height in Graphene/Zinc-Oxide Photodiodes. *Appl. Phys. Lett.* **2013**, *102*, 242114.

(28) Zhu, M.; Li, X.; Guo, Y.; Li, X.; Sun, P.; Zang, X.; Wang, K.; Zhong, M.; Wu, D.; Zhu, H. Vertical Junction Photodetectors Based on Reduced Graphene Oxide/Silicon Schottky Diodes. *Nanoscale* **2014**, *6*, 4909.

(29) Manga, K. K.; Wang, J.; Lin, M.; Zhang, J.; Nesladek, M.; Nalla, V.; Ji, W.; Loh, K. P. High-Performance Broadband Photodetector

Using Solution-Processible PbSe-TiO₂-Graphene Hybrids. *Adv. Mater.* **2012**, *24*, 1697–702.

(30) Zeng, L. H.; Wang, M. Z.; Hu, H.; Nie, B.; Yu, Y. Q.; Wu, C. Y.; Wang, L.; Hu, J. G.; Xie, C.; Liang, F. X.; Luo, L. B. Monolayer Graphene/Germanium Schottky Junction as High-Performance Self-Driven Infrared Light Photodetector. *ACS Appl. Mater. Interfaces* **2013**, *5*, 9362–9366.

(31) Nie, B.; Hu, J. G.; Luo, L. B.; Xie, C.; Zeng, L. H.; Lv, P.; Li, F. Z.; Jie, J. S.; Feng, M.; Wu, C. Y.; Yu, Y. Q.; Yu, S. H. Monolayer Graphene Film on ZnO Nanorod Array for High-Performance Schottky Junction Ultraviolet Photodetectors. *Small* **2013**, *9*, 2872–2879.

(32) Wang, X. M.; Cheng, Z.; Xu, K.; Tsang, H. K.; Xu, J. B. High-Responsivity Graphene/Silicon-Heterostructure Waveguide Photodetectors. *Nat. Photonics* **2013**, *7*, 888–891.

(33) Keem, K.; Kim, H.; Kim, G.-T.; Lee, J. S.; Min, B.; Cho, K.; Sung, M.-Y.; Kim, S. Photocurrent in ZnO Nanowires Grown from Au Electrodes. *Appl. Phys. Lett.* **2004**, *84*, 4376.

(34) Broqvist, P.; Binder, J. F.; Pasquarello, A. Electronic and Structural Properties at Ge/GeO₂ Interfaces: A Density-Functional Investigation. *ECS Trans.* **2010**, *33*, 123–132.

(35) Fu, X. W.; Liao, Z. M.; Zhou, Y. B.; Wu, H. C.; Bie, Y. Q.; Xu, J.; Yu, D. P. Graphene/ZnO Nanowire/Graphene Vertical Structure Based Fast-Response Ultraviolet Photodetector. *Appl. Phys. Lett.* **2012**, *100*, 223114.

(36) Matsubara, H.; Sasada, T.; Takenaka, M.; Takagi, S. Evidence of Low Interface Trap Density in GeO₂/Ge Metal-Oxide-Semiconductor Structures Fabricated by Thermal Oxidation. *Appl. Phys. Lett.* **2008**, *93*, 032104.

(37) Islam, M. R.; Joung, D.; Khondaker, S. I. Schottky Diode via Dielectrophoretic Assembly of Reduced Graphene Oxide Sheets Between Dissimilar Metal Contacts. *New J. Phys.* **2011**, *13*, 035021.

(38) Sun, Z.; Liu, Z.; Li, J.; Tai, G. A.; Lau, S. P.; Yan, F. Infrared Photodetectors Based on CVD-Grown Graphene and PbS Quantum Dots with Ultrahigh Responsivity. *Adv. Mater.* **2012**, *24*, 5878–5883.